

Testing Quasar Unification with Clumpy Wind Models

James H. Matthews^{1,1}, Christian Knigge¹, Nick Higginbottom¹, Knox S. Long², Stuart A. Sim³ and Sam W. Mangham¹

¹School of Physics and Astronomy, University of Southampton, Highfield, Southampton, SO17 1BJ, United Kingdom

²Space Telescope Science Institute, 3700 San Martin Drive, Baltimore, MD, 21218

³School of Mathematics and Physics, Queens University Belfast, University Road, Belfast, BT7 1NN, Northern Ireland, UK

November 12, 2015

ABSTRACT

Various unification schemes have been proposed to interpret the complex phenomenology of quasars and luminous active galactic nuclei (AGN) in terms of a simple axisymmetric picture involving a central black hole, an accretion disc and an associated outflow. Here, we continue our tests of this paradigm by comparing “average” quasar spectra to synthetic spectra of simple biconical disc wind models, using our state-of-the-art Monte Carlo radiative transfer and photoionization code. In particular, we investigate whether clumping of the outflow allows us to produce synthetic spectra in the rest-frame UV that have the characteristics of quasars. We find that a simple treatment of clumping (‘microclumping’) allows for a more realistic X-ray luminosities, while maintaining the ionization state necessary for strong BAL features in the rest-frame UV. We examine the X-ray properties of these simple clumped models and find good agreement with existing X-ray samples of AGN and quasars. The dense, X-ray heated wind produces strong recombination and collisionally excited line emission in, e.g., C IV and Ly α , to emerge at the low inclination, ‘Type 1 quasar-like’ angles. At the highest inclinations, the synthetic spectra possess prominent Mg II and Al III BALs, the absorption features seen in LoBAL quasars. Despite these successes, we are unable to reproduce the remarkably uniform emission line properties seen in BAL and non-BAL quasar composites. This is due to a fundamental constraint arising from the anisotropy of emission from a classical thin disc. Overall, our work suggests that geometric unification involving an accretion disc wind is a promising scenario, but our results pose a number of difficult challenges to such a model.

¹jm8g08@soton.ac.uk

1. Introduction

The spectra of quasars and luminous active galactic nuclei (AGN) typically exhibit a series of strong emission lines with an underlying blue continuum - the so-called ‘*big blue bump*’ (BBB). The BBB is often attributed to emission from a geometrically thin, optically thick accretion disc surrounding the central black hole, similar to that described by Shakura & Sunyaev (1973). In addition to the *inflowing* accreting material, *outflows* are ubiquitous in AGN and quasars (Kellermann et al. 1989; Ganguly & Brotherton 2008). These outflows can take the form of highly collimated radio jets (e.g. Hazard et al. 1963; Potash & Wardle 1980; Perley et al. 1984; Marscher 2006), or mass-loaded ‘winds’ emanating from the accretion disc (Weymann et al. 1991; Turner & Miller 2009). Outflows in AGN offer a potential feedback mechanism through which the central source can affect its environment (King 2003, 2005; Fabian 2012) – feedback that is required in models of galaxy evolution (Springel et al. 2005) and may explain the ‘ $M - \sigma$ ’ relation (Silk & Rees 1998; Häring & Rix 2004).

Perhaps the clearest evidence of outflows in AGN is the blueshifted ($\sim 0.1c$) broad absorption lines (BALs) in the ultraviolet seen in approximately 20% of quasars (Weymann et al. 1991; Reichard et al. 2003; Knigge et al. 2008; Turner & Miller 2009; Allen et al. 2011). The simplest explanation for the incidence of BAL quasars (BALQSOs) is in terms of an accretion disc wind. According to this paradigm, a biconical wind rises from the accretion disc and the BALQSO fraction is associated with the covering factor of the outflow. Polarisation studies expect the wind to be roughly equatorial (Goodrich & Miller 1995; Cohen et al. 1995), although there is also evidence for polar BAL outflows in radio-loud (RL) sources (Zhou et al. 2006).

Due to their ubiquitous nature, disc winds offer a natural explanation for the diverse phenomenology of luminous AGN and QSOs (e.g. Murray et al. 1995; Elvis 2000). Depending on viewing angle, an observer may see a BALQSO or normal ‘Type 1’ quasar. Within this unification framework, the broad-line region (BLR) can correspond either to the dense wind base or clumps embedded in the outflow. Indeed, Elitzur et al. (2014) show that a disc-wind BLR scenario naturally explains the emission line evolution of AGN. A biconical wind model can also readily explain the various sub-classifications of BALQSOs: HiBALQSOs, which only exhibit high ionization line absorption; LoBALQSOs, which also show absorption in lower ionization state species such as Mg II and Al III; and FeLoBALQSOs, which show further absorption in Fe II and III. In unified geometric models, this is generally attributed to ionization stratification of the outflow (e.g. Elvis 2000).

Despite the clear importance of disc winds in shaping quasar and AGN spectra, much of the underlying outflow physics remains highly uncertain. Several possible driving mechanisms have been proposed, including thermal pressure (Weymann et al. 1982; Begelman et al. 1991), magnetocentrifugal forces (Blandford & Payne 1982; Pelletier & Pudritz 1992) and radiation pressure on spectral lines (‘line-driving’; Lucy & Solomon 1970; Shlosman et al. 1985; Murray et al. 1995). Of these, line-driving is possibly the most attractive, as strong absorption lines are already seen in BALQSOs and the X-ray spectra of AGN (Reeves et al. 2003; Pounds & Reeves 2009; Tombesi

et al. 2010). The efficiency of line-driving is crucially dependent on the ionization state of the outflowing plasma, meaning that it is difficult to prevent the wind becoming over-ionized and ‘failing’ in the presence of strong X-rays. Murray et al. (1995) proposed a potential solution: a region of ‘hitchhiking gas’ that could shield the wind from the central X-ray source. An additional or alternative solution is that the wind is clumped (e.g. Hamann et al. 2013) possibly on multiple scale lengths. Local density enhancements could lower the ionization parameter of the plasma while still maintaining the same mass-loss rate and column density.

Evidence for dense substructures in AGN winds is widespread. BALQSOs show complex absorption line profiles (Ganguly et al. 2006; Simon & Hamann 2010) and exhibit variability in these profile shapes (Capellupo et al. 2011, 2012, 2014). AGN generally show variability in X-ray absorption components (e.g. Risaliti et al. 2002) and many models for the BLR consist of clumps embedded in an outflow (Krolik et al. 1981; Emmering et al. 1992; de Kool & Begelman 1995; Cassidy & Raine 1996). Clumping can be caused by magnetic confinement (de Kool & Begelman 1995), or the instabilities inherent to line-driven winds (Lucy & Solomon 1970; MacGregor et al. 1979; Carlberg 1980; Owocki & Rybicki 1984, 1985). Additionally, clumping is required to explain the electron scattering wings of emission lines formed in line-driven hot star winds (Hillier 1991). Complex substructures are also produced in simulations of line-driven outflows in AGN, although on very different scales to line-driven instabilities (Proga et al. 2000; Proga & Kallman 2004; Proga & Kurosawa 2010; Proga et al. 2014). Nevertheless, clumpy winds offer an observationally motivated and theoretically predicted way to lower the ionization state of a plasma, possibly in tandem with a shielding scenario.

We have been engaged in a project to determine whether it is possible to simulate the properties of the spectra of AGN, including BAL QSOs, using simple kinematic prescriptions for biconical disc winds using a Monte Carlo radiative transfer (MCRT) code that calculates the ionization structure of the wind and simulates the spectra from such a system (Sim et al. 2008, 2010; Higginbottom et al. 2013, hereafter H13). The results have been encouraging in the sense that in H13, we showed we could produce simulated spectra that resembled that of BAL QSOs, as long as the luminosity of the central engine was relatively low, of order 10^{43} ergs s $^{-1}$ and the mass loss rate was relatively high, of order the mass accretion rate. However, at higher luminosities, the wind was so ionized that UV absorption lines were not produced. In addition, and in part due to limitations in our radiative transfer code, the model failed to produce spectra with strong emission lines at any inclination angle.

Here we attempt to address both of these issues, by introducing clumping into our model and a more complete treatment of H and He into our radiative transfer calculations. The remainder of this paper is organized as follows: In section 2, we describe some of the important photoionization and MCRT aspects of the code. We then outline the model in section 3, including a description of our clumping implementation and success criteria. Section 4 contains the results from a clumped model, which we discuss results in comparison to observational data. Finally, we summarise our findings in section 5.

2. Ionization and Radiative Transfer

For this study, we use the MCRT code PYTHON we have developed to carry out our radiative transfer and photoionization simulations in non-local thermodynamic equilibrium (non-LTE). The code can be model a variety of disc-wind systems; it has been used with application to accreting white dwarfs (Long & Knigge 2002, hereafter LK02; Noebauer et al. 2010; Matthews et al. 2015, hereafter M15), young-stellar objects (Sim et al. 2005) and quasars/AGN (H13, H14).

The basic premise involves generating photons from an accretion disc and central object, and computing their radiative transfer through an outflow. This outflow is discretized into $n_x \times n_z$ cells in a 2.5D cylindrical geometry with azimuthal symmetry. First, the code gradually converges on the global temperature and ionization structure. Once these “ionization cycles” are complete, then a series of further iterations allow one to obtain a detailed synthetic spectrum. LK02 provides the basic description of the original code; improvements, see especially Sim et al. (2005), H13 and M15, have been described in subsequent reports. We focus here on the specific changes made to improve the ionization calculation and to allow for clumping in the wind.

2.1. Line transfer

Our approach to line transfer is based upon the macro-atom implementation developed by Lucy (2002, 2003), in which the energy flows through the system are described in terms of indivisible energy quanta of radiant or kinetic energy (‘ r –packets’ and ‘ k –packets’ respectively; see also section 3.1). In our case, for reasons of computational efficiency, we adopt the hybrid macro-atom scheme described by M15. In this scheme, the energy packets interact with either two-level ‘simple ions’ or full ‘macro-atoms’. This allows one to treat non-LTE line transfer in radiative equilibrium without approximation for elements that are identified as full macro-atoms, while maintaining the fast ‘two-level’ treatment of resonance lines when elements are identified as simple-ions (see M15). In this study, only H is treated as a macro-atom, because we expect recombination to be important in determining their level populations and resultant line emission, and because we were especially interested in the contribution to AGN spectra of Lyman α . H13 treated all atoms in a two-level approximation.

2.2. Ionization Scheme

Macro-atoms have their ion and level populations derived from MC rate estimators as described by Lucy (2002,2003). Previously (LK02, H13, M15), we used a modified Saha approach to calculate the ionization fractions of simple-ions. As part of this effort, we have now improved PYTHON to explicitly solve the rate equations between ions in non-LTE. This dispenses with a number of small assumptions made in the modified Saha approach, is more numerically stable,

and, in principle, allows the direct addition of extra physical processes that would previously have necessitated approximate treatments.

In order to calculate the photoionization rate, we model the SED in a grid cell using the technique described by H13. In this scheme, the mean intensity, J_ν in a series of n bands is modeled as either a power law or exponential in frequency ν , with the fit parameters deduced from band-limited radiation field estimators. The ionization rate out of ion j can then be written as

$$R_{j,j+1}(J) = n_j \left(C_j n_e + \sum_{band} \int_{\nu_i}^{\nu_{i+1}} \frac{4\pi J_{\nu,i} \sigma_j(\nu)}{h\nu} d\nu \right), \quad (1)$$

where σ_j is the photoionization cross-section, n_e is the electron density and C_j represents the collisional ionization coefficient. The recombination rate *into* ion j is given by

$$R_{j+1,j}(T_e) = (\alpha_{RR}^j + \alpha_{CR}^j) n_{j+1} n_e, \quad (2)$$

where each α^j here is the recombination rate coefficient into the ground state of ion j . The subscripts denote radiative and collisional (three-body) recombination, respectively. T_e is the electron temperature. For simple-ions, we use a dilute Boltzmann equation to calculate the population of level k in ionic stage j ,

$$\frac{n_{jk}}{n_j} = \frac{W g_k}{z_j(T_R)} \exp(-E_k/kT_R). \quad (3)$$

Here z_j is the partition function of ionic stage j , T_R is the effective radiation temperature, E_k is the energy difference between level k and the ground state, and g_k is the statistical weight of level k . We stress that this approximation is not required for ions treated as macro-atoms.

2.3. Physical Processes

We include all free-free, bound-free and bound-bound heating and cooling processes in the model. For radiative transfer purposes we treat electron scattering in the Thomson limit, but take full account of Compton heating and cooling when calculating the thermal balance of the plasma (see H13). Adiabatic cooling is included and represents the only departure from strict radiative equilibrium, but is insignificant in most of the outflow.

2.4. Atomic Data

We use the same atomic data as described by LK02 and since updated by H13 and M15, with the addition of direct (collisional) ionization and recombination data from Dere (2007). Photoionization cross-sections are from TOPBASE (Cunto et al. 1993) and Verner et al. (1996). Radiative recombination rate coefficients are taken from the CHIANTI database version 7.0 (Dere et al. 1997; Landi et al. 2012). We use ground state recombination rates from Badnell (2006) where available,

and otherwise default to calculating recombination rates from the Milne relation. Free-free Gaunt factors are from Sutherland (1998).

3. A Clumpy Biconical Disk Wind Model for Quasars

Our kinematic prescription for a biconical disc wind model follows Shlosman & Vitello (1993), and is described further by LK02, H13 and M15. A schematic is shown in figure 1, with key aspects marked. The general biconical geometry is similar to that invoked by Murray et al. (1995) and Elvis (2000) to explain the phenomenology of quasars and BALQSOs.

3.1. Photon Sources

We include two sources of r-packets in our model: An accretion disc and central X-ray source. The accretion disc is assumed to be geometrically thin, but optically thick. We thus treat the disc as an ensemble of blackbodies with a Shakura & Sunyaev (1973) effective temperature profile. The emergent SED is then determined by the specified accretion rate (\dot{m}) and central BH mass (M_{BH}). All photon sources in our model are opaque, meaning that r-packets which strike them are destroyed. The inner radius of the disc extends to the innermost stable circular orbit (ISCO) of the BH. We assume a Schwarzschild BH with an ISCO at $6 r_G$, where $r_G = GM_{BH}/c^2$ is the gravitational radius. For a $10^9 M_\odot$ black hole, this is equal to 8.8×10^{14} cm or $\sim 10^{-4}$ pc.

The X-ray source is treated as an isotropic sphere at the ISCO, which emits r-packets according to a power law in flux with index α_X , of the form

$$F_X(\nu) = K_X \nu^{\alpha_X}. \quad (4)$$

The normalisation, K_X of this power law is such that it produces the specified 2-10 keV luminosity, L_X . In addition to the disc and X-ray source, the wind is able to reprocess radiation. However, new photon packets are not produced in the wind (as in LK02). Instead, this reprocessing is dealt with by enforcing strict radiative equilibrium (*modulo* adiabatic cooling; see section 2.3) via an indivisible energy packet constraint (see Lucy 2002, M15).

3.2. Kinematics and Geometry

In our model, a biconical disc wind rises from the accretion disc between launch radii r_{min} and r_{max} . The opening angles of the wind are set to θ_{min} and θ_{max} . The poloidal velocity along each individual streamline at a poloidal distance l is then given by

$$v_l = v_0 + [v_\infty(r_0) - v_0] \frac{(l/R_v)^\alpha}{(l/R_v)^\alpha + 1}, \quad (5)$$

where v_0 is the velocity at the base of the streamline, α is an exponent governing how quickly the wind accelerations and R_v is the ‘acceleration length’, defined as the distance at which the outflow reaches half of its terminal velocity, v_∞ . The terminal velocity is set to a fixed multiple of the escape velocity, v_{esc} , at the base of the streamline (radius r_0). The rotational velocity, v_ϕ , is initially Keplerian ($v_k = [GM/r_0]^{1/2}$), and the wind conserves specific angular momentum, such that

$$v_\phi r = v_k r_0. \quad (6)$$

The velocity law is crucial in determining the output spectra, as it affects not only the projected velocities along the line of sight, but also the density and ionization state of the outflow. A wind that accelerates more slowly will have a denser wind base with correspondingly different ionization and emission characteristics.

3.3. A First Approximation for Clumping

Our previous modelling efforts assumed a smooth outflow, in which the density at a given point was determined only by the kinematic parameters and mass loss rate. However, as already discussed, AGN winds exhibit significant substructure – the outflow is expected to be *clumpy*, rather than smooth, and probably on a variety of scales. Implementing a treatment of clumping is challenging, for two main reasons. First, there are significant computational difficulties associated with adequately resolving and realistically modelling a series of small scale, high density regions with a MCRT code. Second, the addition of multiple additional degrees of freedom in the model results in significantly wider parameter space. Unfortunately, the physical scale lengths and density contrasts associated with these parameters cannot be well-constrained from observations.

To allow for clumping in our outflow we adopt a simple approximation used successfully in stellar wind modelling, known as *microclumping* (Hamann & Koesterke 1998; Hamann et al. 2008)(MORE REFS). The key assumption is that typical clump sizes are much smaller than the typical photon mean free path, and thus the clumps are both geometrically and optically thin. This approach allows one to introduce a ‘volume filling factor’, f_V . The intra-clump medium is assumed to be a vacuum, so the density of the clumps is then multiplied by the “density enhancement” $D = 1/f_V$. Opacities, κ , and emissivities, ϵ , can then be expressed as

$$\kappa = f_V \kappa_C(D); \quad \epsilon = f_V \epsilon_C(D). \quad (7)$$

Here the subscript C denotes that the quantity is calculated using the enhanced density in the clump. The resultant effect is that *linear* processes, such as electron scattering, are unchanged, as f_V and D will cancel out. However, any quantity which scales with the *square* of density, such as collisional excitation or recombination, will increase by a factor of D .

Clumping the wind has an important effect on the ionization state and has been proposed as a solution to the so-called ‘over-ionization problem’ in disc winds (Hamann et al. 2013). This is

the main motivation for incorporating microclumping into our model. This treatment is first-order; it does not adequately represent the complex substructures and stratifications in ionization state we expect in AGN outflows. Nevertheless, clumping is clearly important in these flows, and this parameterization allows a simple estimate for the effect clumping might have on the ionization state and emergent line emission.

3.4. The Simulation Grid: Arriving at a next-generation model

Using this prescription, we conducted a limited parameter search over a 5-dimensional parameter space involving the variables r_{min} , θ_{min} , f_V , α and R_v . The grid points are shown in table 1. The aim here was to first fix M_{BH} and \dot{m} to their H13 values, and increase L_X to 10^{45} erg s $^{-1}$ (a more realistic value for a quasar of $10^9 M_\odot$ and an eddington fraction of 0.2; see section 4.3). We then evaluated these models based on the following criteria:

- Does the model avoid over-ionization and thus produce UV absorption lines with $BI > 0$ at $\sim 20\%$ of viewing angles?
- Does significant line emission emerge at low inclinations, with $EW \sim 40\text{\AA}$ in C iv?
- Do H recombination lines appear in the spectrum, $EW \sim 50\text{\AA}$ in Ly α ?
- Do a small subset of BAL angles produce LoBAL features?
- Does the model compare favourably to quasar composite spectra?

In this section, we present one of the most promising models and discuss the various successes and failures with respect to the above criteria. This allows us to gain insight into fundamental geometrical and physical constraints and assess the potential for unification. The full grid, including output synthetic spectra and plots can be found at [jhmatthews.github.io/quasar-wind-grid/](https://github.com/jhmatthews/quasar-wind-grid/).

Parameter	Grid Point Values			
r_{min}	$6r_g$	$60r_g$	$300r_g$	
θ_{min}	40°	55°	70°	
R_v	10^{18}cm	10^{19}cm		
α	0.5	0.6	0.75	1.5
f_V	0.01	0.1	1	

Table 1: The grid points used in the parameter search.

4. Results and Discussion

Here we describe the results from our next-generation model, and discuss these results in the context of the criteria presented in section 3.4. The parameters of this model are shown in table 2. Parameters differing from the benchmark model of H13 are highlighted with an asterisk. In this section, we examine the physical conditions of the flow, and present the synthetic spectra, before comparing the X-ray properties of this particular model to samples of quasars and luminous AGN. We also examine trends with inclination in the synthetic spectra, both in terms of the range of ionization states of the absorption lines and equivalent widths of the emission lines.

4.1. Physical Conditions and Ionization State

Figure 2 shows the physical properties of the wind. The wind rises slowly from the disc at first, with clumped densities of $n_H \sim 10^{11} \text{ cm}^{-3}$ close to the disc plane. The flow then accelerates over a scale length of $R_V = 10^{19} \text{ cm}$ up to a terminal velocity equal to the escape velocity at the streamline base ($\sim 10,000 \text{ km s}^{-1}$). This gradual acceleration means that the wind exhibits a stratified ionization structure, with low ionization material in the base of the wind giving way to highly ionized plasma further out. This is illustrated in figure 2 by the panels showing the ion fraction $F = n_j/n_{tot}$ of some important ions. By clumping the wind, we are able to produce the range of ionization states observed in quasars and BALQSOs, while adopting a realistic 2 – 10 keV X-ray luminosity of $L_X = 10^{45} \text{ ergs s}^{-1}$. Without clumping, this wind would be over-ionized to the extent that opacities in e.g., C IV would be entirely negligible (see H13).

One common way to quantify the ionization state of a plasma is through the ionization parameter, U_H , given by

$$U_H = \frac{4\pi}{n_H c} \int_{13.6\text{eV}}^{\infty} \frac{J_\nu d\nu}{h\nu}. \quad (8)$$

where n_H is the local number density of H, and ν denotes photon frequency. Shown in figure 2, the ionization parameter is a useful measure of the global ionization state, as it represents the ratio of the number density of H ionizing photons to the local H density. It is, however, a poor representation of the ionization state of species such as C IV as it encodes no information about the shape of the SED. In our case, the X-ray photons are dominant in the photoionization of the UV resonance line ions. This explains why a factor of 100 increase in X-ray luminosity requires a clumping factor of 0.01, even though the value of U_H decreases by only a factor of ~ 10 compared to H13.

Clumping also causes the total line luminosity to increase dramatically, as recombination and collisional excitation are both proportional to density squared. This line emission typically emerges on the edge of the wind nearest the central source. The location of the line emitting regions is dependent on the ionization state, as well as the X-rays heating the plasma. The radii of these emitting regions is important, and can be compared to observations. The line luminosities shown

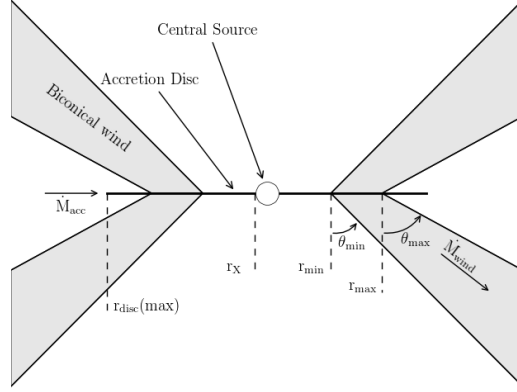


Fig. 1.— A cartoon showing the geometry and some key parameters of our biconical wind model.

Next-generation Model	Value Parameters
M_{BH}	$1 \times 10^9 M_\odot$
\dot{M}_{acc}	$5 M_\odot yr^{-1} \simeq 0.2 \dot{M}_{Edd}$
α_X	-0.9
L_X	$10^{45} \text{ ergs s}^{-1*}$
$r_{disc}(min) = r_X$	$6r_g = 8.8 \times 10^{14} \text{ cm}$
$r_{disc}(max)$	$3400r_g = 5 \times 10^{17} \text{ cm}$
\dot{M}_{wind}	$5 M_\odot yr^{-1}$
r_{min}	$300r_g = 4.4 \times 10^{16} \text{ cm}$
r_{max}	$600r_g = 8.8 \times 10^{16} \text{ cm}$
θ_{min}	70.0°
θ_{max}	82.0°
λ	0
$v_\infty(r_0)$	$v_{esc}(r_0)$
R_v	10^{19} cm^*
α	0.6^*
f_V	0.01^*
n_x	100
n_z	200

Table 2: Wind geometry parameters used in the model.

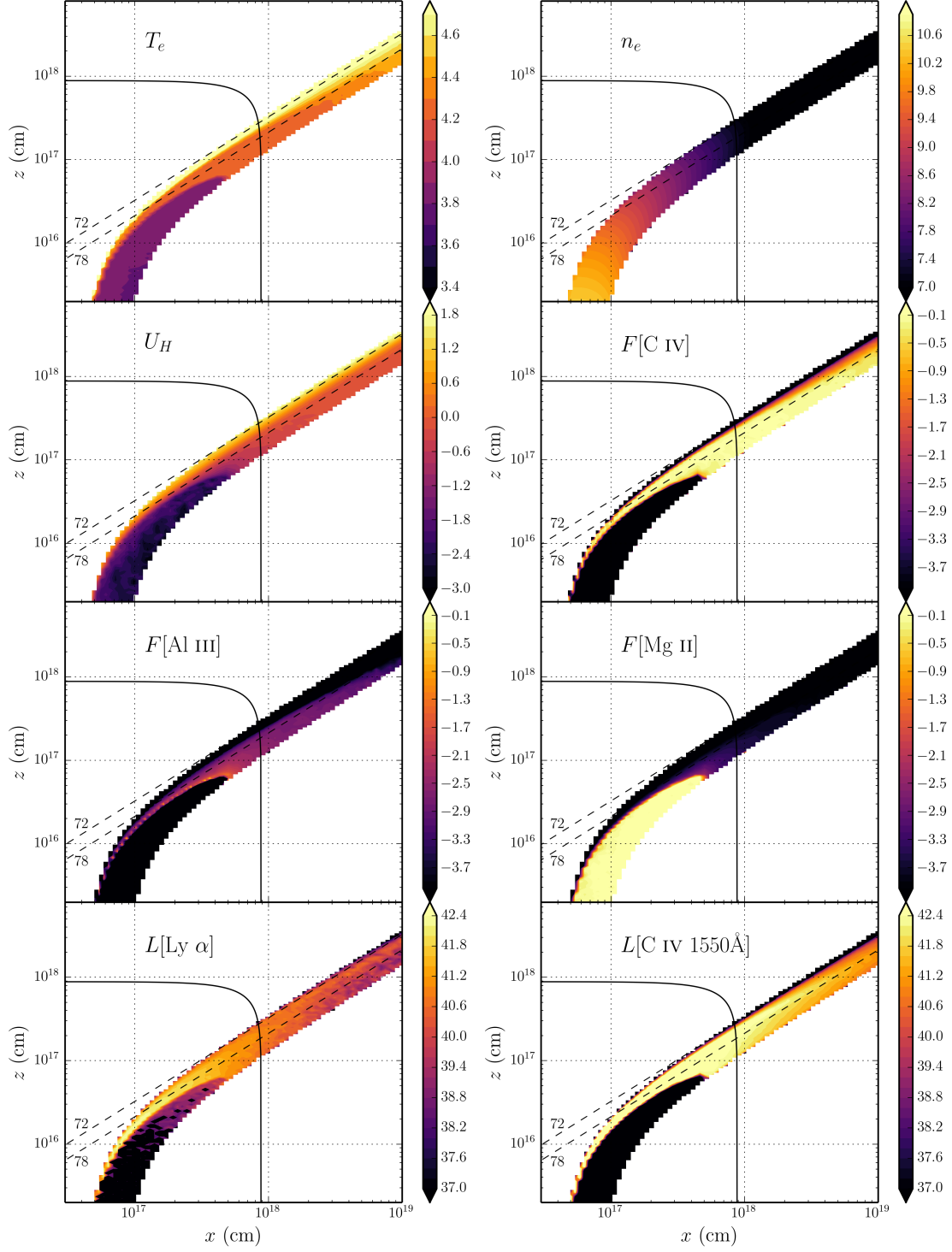


Fig. 2.— Contour plots showing the logarithm of some important physical properties of the outflow. Symbols are defined in the text. The solid black line marks a sphere at $1000 r_G$. The dotted lines show the 72° and 78° sightlines to the centre of the system, and illustrate that different sightlines intersect material of different ionization states. The line luminosities represent the luminosity of photons escaping the Sobolev region for each line. These photons do not necessarily escape to infinity.

in the figure correspond to the luminosity in ergs s^{-1} of photons escaping the Sobolev region for each line. This is equivalent to $\beta_{ul}n_uA_{ul}$, where the three quantities represent the Sobolev escape probability, upper level number density and Einstein A coefficient for the line. As shown in figure 2, the C IV line in our model is typically formed between $100 - 1000 r_G$ ($\sim 10^{17} - 10^{18}$ cm). This is in rough agreement with the reverberation mapping results of Kaspi (2000) for the $2.6 \times 10^9 M_\odot$ quasar S5 0836+71, and also compares favourably with microlensing measurements of the size of the C IV emission line region in the BALQSO H1413+117 (O’Dowd et al. 2015).

4.2. Synthetic Spectra: Comparison to Observations

Figure 3 shows the synthetic spectrum in the UV from our model. To assess the ability of the model to match real quasar spectra, we also show *Sloan Digital Sky Survey* (SDSS) quasar and BALQSO composites from Reichard et al. (2003), normalised to the flux at 2000\AA in each panel. We show a cartoon illustrating how geometric effects determine the output spectra in figure 4.

4.2.1. Broad absorption lines (‘BALQSO-like’ angles)

The UV spectrum is characterised by strong BAL profiles at high inclinations ($> 70^\circ$). This highlights the first success of our model: clumping means the correct ionization state is maintained in the presence of strong X-rays, allowing large resonance line opacities. At the highest inclinations, the cooler, low ionization material at the base of the wind starts to intersect the line of sight. This produces multiple absorption lines in species such as Mg II, Al III and Fe II. The potential links to LoBALQSOs and FeLoBALQSOs are discussed in section 2.4. Clearly, the absorption lines in the synthetic spectra at BALQSO-like angles do not match the composites; this is *not* due to a failure of our model, but rather because a geometric mean BALQSO composite spectrum tends to wash out the broad absorption features due to the wide range of absorption characteristics. To demonstrate this, we show a comparison to a *Hubble Space Telescope* STIS spectrum of the high BALnicity BALQSO PG0946+301 (Arav et al. 2000) in figure 5.

The high ionization BAL profiles are often saturated, and the location in velocity space of the strongest absorption in the profile varies with inclination. At the lowest inclination BAL sightlines, the strongest absorption occurs at the red edge, whereas at higher inclinations (and for the strongest BALs) the trough has a sharp edge at the terminal velocity. This offers one potential explanation for the wide range of BALQSO absorption line shapes (see e.g. Trump et al. 2006; Knigge et al. 2008, Filiz Ak et al. 2014). In addition, the line profile shape is strongly dependent on the density, ionization and velocity profiles intersected by the line of sight. Thus, small tweaks of the velocity law and angular distributions of streamlines can dramatically alter the shape of the line.

Nonblack saturation is observed in the absorption troughs of BALQSOs (Arav et al. 1999b,a). This can be caused either by partial covering of the continuum source or by scattered contributions

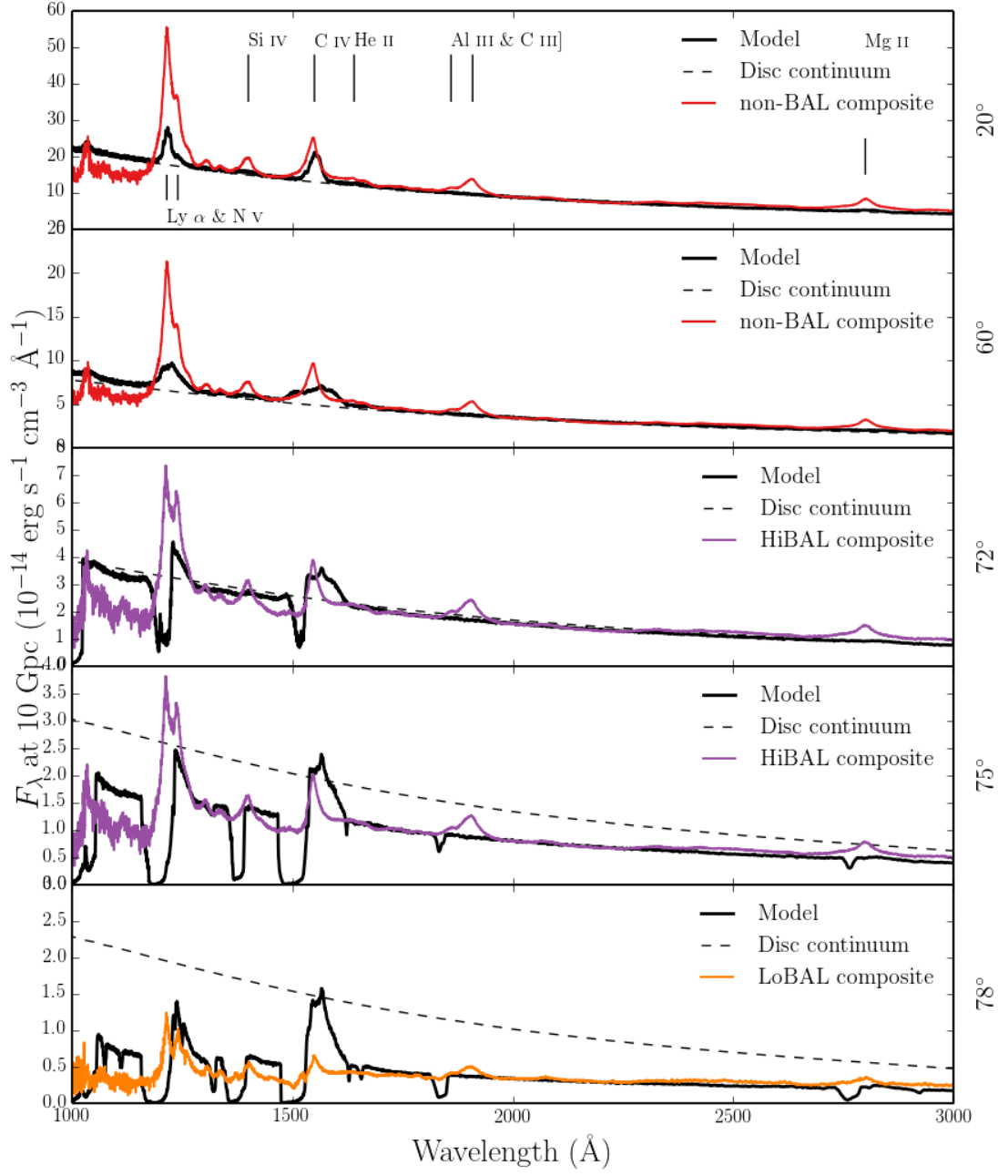


Fig. 3.— Synthetic spectra at five viewing angles in our model. The coloured lines show different quasar and BAL quasar composites, and the dotted line shows a disc only continuum to show the effect of the outflow on the continuum level.

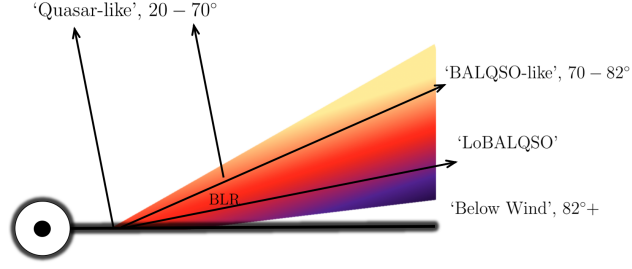


Fig. 4.— A cartoon describing the broad classes of sightline in our model, illustrating how geometric effects lead to the different emergent spectra. The colour gradient is approximate, but indicates the stratified ionization structure, from highly ionized (yellow) to low ionization (purple) material.

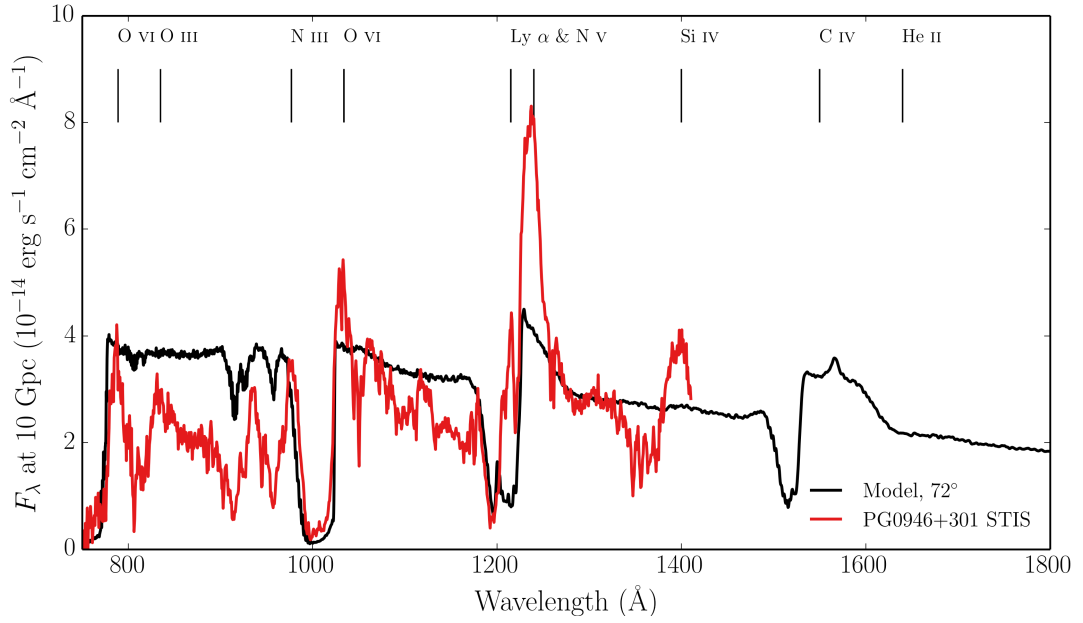


Fig. 5.— Synthetic spectra at 72° compared to an HST STIS spectrum of PG0946+301 (Arav et al. 2000). The spectrum is scaled to the flux at 1300\AA for direct comparison.

to the BAL troughs, necessarily from an opacity source not cospatial with the BAL forming region. The scattered light explanation is supported by spectropolarimetry results (Lamy & Hutsemékers 2000). Our spectra do not show nonblack saturation. Instead, we find black, saturated troughs at angles $i > 73^\circ$, and the BALs are non-saturated at lower inclinations. The reasons for this are readily apparent. First, the microclumping assumption does not allow for porosity in the wind, meaning that it does not naturally produce a partial covering absorber. To do this, an alternative approach such as *macroclumping* would be required (e.g. Šurlan et al. 2012; Hamann et al. 2008). Second, our wind does not have a significant scattering contribution along sightlines which do not pass through the BAL region, meaning that any scattered component to the BAL troughs is absorbed by line opacity. This suggests that either the scattering cross-section of the wind must be increased (with higher mass loss rates or covering factors), or that an additional source of electron opacity is required, potentially in a polar direction above the disc.

4.2.2. Broad emission lines (‘quasar-like’ angles)

We find significant collisionally excited line emission emerges at low inclinations in the synthetic spectra, particular in the C IV line. The improved treatment of recombination also results in a strong Ly α line. In the context of unification, this is a promising result, and shows that a biconical wind can produce significant emission at ‘quasar-like’ angles. The spectra do not contain the strong C III] 1909Å line seen in the quasar composite spectra. This is because we do not yet treat C as a full macro-atom with a full collisional rates between forbidden or semi-forbidden transitions, as would be required. The critical density of the C III] 1909Å line is $n_e \sim 10^{9.5} \text{ cm}^{-3}$ (Wei 1988), which is higher than much of the outer portion of our wind. We therefore expect a model with these parameters to produce a C III] 1909Å line with a proper treatment.

The model produces strong emission lines in C IV, N V and Ly α , as well as a weak Mg II line. The shapes and widths of these lines match the composites fairly well. However, the line-to-continuum ratios at low inclinations in our model are significantly weaker than the quasar composites. Increasing the density of the outflow, by altering the mass loss rate or velocity law, can produce more line emission. However, the red wing of the BAL profiles is generally stronger than seen in BALQSO spectra and composites. This illustrates a fundamental problem with a geometric unification model such as this: that the line-to-continuum ratios at high inclinations are significantly affected by disc foreshortening and limb darkening. The angular distribution of the disc radiation is clearly crucially important in determining the emergent line ratios.

4.2.3. The Angular Distribution of Line And Continuum Emission

In order to quantitatively assess how emission lines change with inclination when blue-shifted absorption may affect the line profile, we define the ‘red wing equivalent width’ ($W_{\lambda,RW}$) as

$$W_{\lambda,RW} = \int_{\lambda_0}^{\lambda'} \left(1 - \frac{F_{\lambda}}{F_0} \right) d\lambda \quad (9)$$

where F_0 is the continuum flux and the integral is calculated from λ_0 , line centre, to a wavelength λ' where the flux has returned to the continuum level. This quantity is shown as a function of inclination in figure 5 for the C IV and Mg II UV lines. We also plot show the $W_{\lambda,RW}$ expected from isotropic line emission and a foreshortened and limb darkened disc as well as 1/2 equivalent widths from DiPompeo et al. (2012).

BALQSOs and quasars generally possess very similar emission line properties (e.g. Weymann et al. 1991; Reichard et al. 2003). Clearly, the variation with inclination in our models is far greater than than the variation between, and standard deviation within, quasar and BALQSO samples. This presents a challenge to our model, as well as the geometric unification picture in general. One obvious potential solution is to hypothesize a more isotropic distribution for the emergent condition than predicted by a classical thin disc. General relativistic effects – specifically, light bending and relativistic beaming – can cause the accretion disc SED to become more isotropic (e.g. Zhang et al. 1997; Muñoz-Darias et al. 2013). However, we have verified using AGNSPEC (Hubeny et al. 2000, 2001; Hubeny & Hubeny 1997) that this effect is small in the UV and optical wavelength regimes, and the disc is still anisotropic.

Reprocessing by an extended outflow may also cause a more isotropic continuum to emerge. Hints that light scattered off a spatially extended wind may contribute significantly to the emergent continuum come from radiative transfer simulations (Sim et al. 2012) and microlensing observations (Sluse et al. 2015). However, neither of these examples have sufficient reprocessing efficiencies to compensate for the disc anisotropy in this case. An alternative explanation is that the BLR has the same angular distribution of emission as the accretion disc. Indeed, Risaliti et al. (2011) find that EW distributions in quasars are consistent with anisotropic emission from optically thick, disc-like structures for *both* the continuum source and BLR. If this is the case, it has a dramatic affect on the intrinsic BAL fraction inferred from flux-limited samples (Goodrich 1997; Krolik & Voit 1998).

It is also possible that the equatorial paradigm invoked from early polarisation studies (Goodrich & Miller 1995; Cohen et al. 1995; Brotherton et al. 2006) is an over-simplification, or is merely incorrect. High brightness temperatures in some RL BALQSOs imply polar outflows (Zhou et al. 2006) and Bruni et al. (2012) find that RL BALQSOs possess similar radio spectral indices to normal RL quasars, suggestive of comparable inclinations. In addition, Marin & Goosmann (2013) find a bending angle of $\sim 45^\circ$ is required to explain the polarisation dichotomy of type 1 and 2 AGN using an Elvis-type wind model (Elvis 2000). It is therefore possible that type 1 quasars and BALQSOs are generally viewed from a fairly narrow range of angles ($\sim 0-45^\circ$), or that *both*

evolutionary and geometric explanations are required. We suggest that future modelling should include predictions of polarisation signatures from a detailed radiative transfer simulation, allowing direct comparison with spectropolarimetry of BALQSOs.

4.3. X-ray Properties and Broadband SEDs

One of the main motivations for including a treatment of clumping was to avoid over-ionization of the wind in the presence of strong X-rays. Having verified that strong BALs appear in the synthetic spectra, it is also important to assess whether the X-ray properties of this next-generation model agree well with quasar and BALQSO samples for the relevant inclinations.

Figure 7 shows the emergent monochromatic luminosity (L_ν) at 2 keV and plotted against L_ν at 2500Å for a number of different viewing angles in our model. The monochromatic luminosities are calculated from the synthetic spectra and thus include the effects of wind reprocessing and attenuation. In addition to model outputs, we also show the BALQSO sample of Saez et al. (2012) and luminous AGN and quasar samples from Steffen et al. (2006). The best fit relation from Steffen et al. (2006) is also shown. For low inclination, ‘quasar-like’ viewing angles, we now find excellent agreement with AGN samples. The gradient from 20° to 60° in our models is caused by a combination of disc foreshortening/limb-darkening (resulting in a lower L_{2500} for higher inclinations) and the fact that the disk is opaque, and thus the X-ray source subtends a smaller solid angle at high inclinations (resulting in a lower L_{2keV} for higher inclinations).

The low inclination, ‘BALQSO-like’ viewing angles show moderate agreement with the data, and are X-ray weak due to bound-free and electron scattering opacities in the wind. Typically, BALQSOs show strong X-ray absorption with columns of $N_H \sim 10^{23} \text{ cm}^{-2}$ (Green & Mathur 1996; Mathur et al. 2000; Green et al. 2001; Grupe et al. 2003). This is often cited as evidence that the BAL outflow is shielded from the X-ray source, especially as sources with strong X-ray absorption tend to exhibit deep BAL troughs and high outflow velocities (Brandt et al. 2000; Laor & Brandt 2002; Gallagher et al. 2006). Our results imply that the clumpy BAL outflow itself can be responsible for the strong X-ray absorption, and supports Hamann et al.’s (2013) suggestion that this explains the weaker X-ray absorption in mini-BALs compared to BALQSOs.

Our models slightly over-predict the emergent X-ray luminosity at BAL angles, although we are limited by poor sample sizes. If BALQSOs were *intrinsically* X-ray weak (as suggested by, e.g. Morabito et al. 2013), our isotropic assumption for the X-ray source would be incorrect. A polar-biased X-ray source would result in a lower clumping factor being required in our model. Our specific wind prescription will also affect the opacities, densities and resultant ionization structure, which can change the absorption characteristics and resultant luminosities. Nevertheless, our input X-ray spectrum now reproduces the X-ray properties of a luminous quasar as an output, and at least some BAL angles match the observations. This satisfies the first-order requirement for the X-ray properties of a unified quasar model.

4.4. LoBALs and ionization stratification

At certain sightlines, the synthetic spectra exhibit blue-shifted BALs in Al III and Mg II– the absorption lines seen in LoBALQSOs, and we even see absorption in Fe II at the highest inclinations. Line profiles in velocity space for C IV, Al III and Mg II, are shown in figure 8 for a range of BALQSO viewing angles. We find that ionization stratification of the wind causes lower ionization material to have a smaller covering factor, as demonstrated by figures 2 and 8. This confirms the behaviour expected from a unification model such as Elvis (2000). LoBALs are only present at viewing angles close to edge-on ($i > 75^\circ$), as predicted by polarisation results (Brotherton et al. 1997). As observed in a BALQSO sample by Filiz Ak et al. (2014), we find that BAL troughs are wider and deeper when low ionization absorption features are present, and high ionization lines have higher blue-edge velocities than the low ionization species. There is also a correlation between the strength of LoBAL features and the amount of continuum attenuation at that sightline, particularly blueward of the Lyman edge as the low ionization base intersects the line-of-sight. A model such as this therefore predicts that LoBALQSOs and FeLoBALQSOs have stronger Lyman edge absorption and are more Compton-thick than HiBALQSOs and Type 1 quasars. An edge-on scenario also offers a potential explanation for the rarity of LoBAL and FeLoBAL quasars, due to a foreshortened and attenuated continuum, although, as noted in section ??, BAL fraction inferences are fraught with complex selection effects.

5. Summary

We have carried out MCRT simulations using a simple prescription for a biconical disc wind, with the aim of expanding on the work of H13 and assessing the viability of such a model for geometric unification of quasars. We find the following main points:

1. We have introduced a first-order treatment of clumping in our model, and found that it can now maintain the required ionization state while agreeing well with the X-ray properties of AGN/QSOs.
2. We have shown that the degree of ionization stratification in the model is sufficient that LoBAL line profiles are seen at a subset of viewing angles, and Fe II absorption is seen at particularly high inclinations.
3. We find that clumping also causes a significant increase in the strength of the emission lines produced by the model. This is true both of collisionally excited resonance lines (such as C IV, N V) and recombination lines (such as Ly α , H α and the Balmer series).
4. The line EWs in our models increase with inclination. BAL and non-BAL quasar composites have comparable EWs, so our model fails to reproduce this behaviour. This is due to a

fundamental constraint discussed further in section ?? . If the BLR emits fairly isotropically then for a foreshortened, limb-darkened classical thin accretion disc it is simply not possible to achieve line ratios at low inclinations that are comparable to those at high inclinations. This is a robust conclusion which is independent of the assumed BLR geometry and size.

Our work confirms a number of expected outcomes from a geometric unification model, and suggests that a simple biconical geometry such as this can come close to explaining much of the phenomenology of quasars. Nevertheless, our conclusions pose a clear challenge to the current disc wind unification picture.

Acknowledgements

The work of JHM, SWM, NSH and CKL is supported by the Science and Technology Facilities Council (STFC), via two studentships and a consolidated grant, respectively. CK also acknowledges a Leverhulme fellowship. We would like to thank Omer Blaes, Ivan Hubeny and Shane Davis for their assistance with AGNSPEC. We are grateful to Mike Brotherton, Mike DiPompeo, Sebastien Hoenig and Frederic Marin for helpful correspondence regarding polarisation measurements and orientation indicators. We would also like to thank Daniel Proga, Daniel Capellupo, Sam Connolly and Dirk Grupe for useful discussions. Simulations were conducted using PYTHON version 80, and made use of the IRIDIS High Performance Computing Facility at the University of Southampton. Figures were produced using the `matplotlib` plotting library (Hunter 2007).

REFERENCES

- Allen J. T., Hewett P. C., Maddox N., Richards G. T., Belokurov V., 2011, *MNRAS* 410, 860
- Arav N., Becker R. H., Laurent-Muehleisen S. A., Gregg M. D., White R. L., Brotherton M. S., de Kool M., 1999a, *ApJ* 524, 566
- Arav N., Korista K. T., de Kool M., Junkkarinen V. T., Begelman M. C., 1999b, *ApJ* 516, 27
- Badnell N. R., 2006, *ApJs* 167, 334
- Begelman M., de Kool M., Sikora M., 1991, *ApJ* 382, 416
- Blandford R. D., Payne D. G., 1982, *MNRAS* 199, 883
- Brandt W. N., Laor A., Wills B. J., 2000, *ApJ* 528, 637
- Brotherton M. S., De Breuck C., Schaefer J. J., 2006, *MNRAS* 372, L58
- Brotherton M. S., Tran H. D., van Breugel W., Dey A., Antonucci R., 1997, *ApJ Letters* 487, L113

- Bruni G., Mack K.-H., Salerno E., Montenegro-Montes F. M., Carballo R., Benn C. R., González-Serrano J. I., Holt J., Jiménez-Luján F., 2012, *A&A* 542, A13
- Capellupo D. M., Hamann F., Barlow T. A., 2014, *MNRAS* 444, 1893
- Capellupo D. M., Hamann F., Shields J. C., Rodríguez Hidalgo P., Barlow T. A., 2011, *MNRAS* 413, 908
- Capellupo D. M., Hamann F., Shields J. C., Rodríguez Hidalgo P., Barlow T. A., 2012, *MNRAS* 422, 3249
- Carlberg R. G., 1980, *ApJ* 241, 1131
- Cassidy I., Raine D. J., 1996, *A&A* 310, 49
- Cohen M. H., Ogle P. M., Tran H. D., Vermeulen R. C., Miller J. S., Goodrich R. W., Martel A. R., 1995, *ApJ Letters* 448, L77
- Cunto W., Mendoza C., Ochsenbein F., Zeppen C. J., 1993, *A&A* 275, L5
- de Kool M., Begelman M. C., 1995, *ApJ* 455, 448
- Dere K. P., 2007, *A&A* 466, 771
- Dere K. P., Landi E., Mason H. E., Monsignori Fossi B. C., Young P. R., 1997, *A&As* 125, 149
- DiPompeo M. A., Brotherton M. S., Cales S. L., Runnoe J. C., 2012, *MNRAS* 427, 1135
- Elitzur M., Ho L. C., Trump J. R., 2014, *MNRAS* 438, 3340
- Elvis M., 2000, *ApJ* 545, 63
- Emmering R. T., Blandford R. D., Shlosman I., 1992, *ApJ* 385, 460
- Fabian A. C., 2012, *ARAA* 50, 455
- Filiz Ak N., Brandt W. N., Hall P. B., Schneider D. P., Trump J. R., Anderson S. F., Hamann F., Myers A. D., Pâris I., Petitjean P., Ross N. P., Shen Y., York D., 2014, *ApJ* 791, 88
- Gallagher S. C., Brandt W. N., Chartas G., Priddey R., Garmire G. P., Sambruna R. M., 2006, *ApJ* 644, 709
- Ganguly R., Brotherton M. S., 2008, *ApJ* 672, 102
- Ganguly R., Sembach K. R., Tripp T. M., Savage B. D., Wakker B. P., 2006, *ApJ* 645, 868
- Goodrich R. W., 1997, *ApJ* 474, 606
- Goodrich R. W., Miller J. S., 1995, *ApJ Letters* 448, L73

- Green P. J., Aldcroft T. L., Mathur S., Wilkes B. J., Elvis M., 2001, *ApJ* 558, 109
- Green P. J., Mathur S., 1996, *ApJ* 462, 637
- Grupe D., Mathur S., Elvis M., 2003, *AJ* 126, 1159
- Hamann F., Chartas G., McGraw S., Rodriguez Hidalgo P., Shields J., Capellupo D., Charlton J., Eracleous M., 2013, *MNRAS* 435, 133
- Hamann W.-R., Koesterke L., 1998, *A&A* 335, 1003
- Hamann W.-R., Oskinova L. M., Feldmeier A., 2008, in W.-R. Hamann, A. Feldmeier, L. M. Oskinova (eds.), *Clumping in Hot-Star Winds*, 75
- Häring N., Rix H.-W., 2004, *ApJ Letters* 604, L89
- Hazard C., Mackey M. B., Shimmins A. J., 1963, *Nature* 197, 1037
- Higginbottom N., Knigge C., Long K. S., Sim S. A., Matthews J. H., 2013, *MNRAS* 436, 1390
- Hillier D. J., 1991, *A&A* 247, 455
- Hubeny I., Agol E., Blaes O., Krolik J. H., 2000, *ApJ* 533, 710
- Hubeny I., Blaes O., Krolik J. H., Agol E., 2001, *ApJ* 559, 680
- Hubeny I., Hubeny V., 1997, *ApJ Letters* 484, L37
- Hunter J. D., 2007, *Computing In Science & Engineering* 9(3), 90
- Kellermann K. I., Sramek R., Schmidt M., Shaffer D. B., Green R., 1989, *AJ* 98, 1195
- King A., 2003, *ApJ Letters* 596, L27
- King A., 2005, *ApJ Letters* 635, L121
- Knigge C., Scaringi S., Goad M. R., Cottis C. E., 2008, *MNRAS* 386, 1426
- Krolik J. H., McKee C. F., Tarter C. B., 1981, *ApJ* 249, 422
- Krolik J. H., Voit G. M., 1998, *ApJ Letters* 497, L5
- Lamy H., Hutsemékers D., 2000, *A&A* 356, L9
- Landi E., Del Zanna G., Young P. R., Dere K. P., Mason H. E., 2012, *ApJ* 744, 99
- Laor A., Brandt W. N., 2002, *ApJ* 569, 641
- Long K. S., Knigge C., 2002, *ApJ* 579, 725

- Lucy L. B., 2002, *A&A* 384, 725
- Lucy L. B., 2003, *A&A* 403, 261
- Lucy L. B., Solomon P. M., 1970, *ApJ* 159, 879
- MacGregor K. B., Hartmann L., Raymond J. C., 1979, *ApJ* 231, 514
- Marin F., Goosmann R. W., 2013, *MNRAS* 436, 2522
- Marscher A. P., 2006, in P. A. Hughes, J. N. Bregman (eds.), *Relativistic Jets: The Common Physics of AGN, Microquasars, and Gamma-Ray Bursts*, Vol. 856 of *American Institute of Physics Conference Series*, p. 1
- Mathur S., Green P. J., Arav N., Brotherton M., Crenshaw M., deKool M., Elvis M., Goodrich R. W., Hamann F., Hines D. C., Kashyap V., Korista K., Peterson B. M., Shields J. C., Shlosman I., van Breugel W., Voit M., 2000, *ApJ Letters* 533, L79
- Matthews J. H., Knigge C., Long K. S., Sim S. A., Higginbottom N., 2015, *MNRAS* 450, 3331
- Morabito L. K., Dai X., Leighly K. M., Sivakoff G. R., Shankar F., 2013, *ArXiv e-prints*
- Muñoz-Darias T., Coriat M., Plant D. S., Ponti G., Fender R. P., Dunn R. J. H., 2013, *MNRAS* 432, 1330
- Murray N., Chiang J., Grossman S. A., Voit G. M., 1995, *ApJ* 451, 498
- Noebauer U. M., Long K. S., Sim S. A., Knigge C., 2010, *ApJ* 719, 1932
- O’Dowd M. J., Bate N. F., Webster R. L., Labrie K., Rogers J., 2015, *ArXiv e-prints*
- Owocki S. P., Rybicki G. B., 1984, *ApJ* 284, 337
- Owocki S. P., Rybicki G. B., 1985, *ApJ* 299, 265
- Pelletier G., Pudritz R. E., 1992, *ApJ* 394, 117
- Perley R. A., Dreher J. W., Cowan J. J., 1984, *ApJ Letters* 285, L35
- Potash R. I., Wardle J. F. C., 1980, *ApJ* 239, 42
- Pounds K. A., Reeves J. N., 2009, *MNRAS* 397, 249
- Proga D., Jiang Y.-F., Davis S. W., Stone J. M., Smith D., 2014, *ApJ* 780, 51
- Proga D., Kallman T. R., 2004, *ApJ* 616, 688
- Proga D., Kurosawa R., 2010, in L. Maraschi, G. Ghisellini, R. Della Ceca, F. Tavecchio (eds.), *Accretion and Ejection in AGN: a Global View*, Vol. 427 of *Astronomical Society of the Pacific Conference Series*, 41

- Proga D., Stone J. M., Kallman T. R., 2000, *ApJ* 543, 686
- Reeves J. N., O’Brien P. T., Ward M. J., 2003, *ApJ Letters* 593, L65
- Reichard T. A., Richards G. T., Hall P. B., Schneider D. P., Vanden Berk D. E., Fan X., York D. G., Knapp G. R., Brinkmann J., 2003, *AJ* 126, 2594
- Risaliti G., Elvis M., Nicastro F., 2002, *ApJ* 571, 234
- Risaliti G., Salvati M., Marconi A., 2011, *MNRAS* 411, 2223
- Shakura N. I., Sunyaev R. A., 1973, *A&A* 24, 337
- Shlosman I., Vitello P., 1993, *ApJ* 409, 372
- Shlosman I., Vitello P. A., Shaviv G., 1985, *ApJ* 294, 96
- Silk J., Rees M. J., 1998, *A&A* 331, L1
- Sim S. A., Drew J. E., Long K. S., 2005, *MNRAS* 363, 615
- Sim S. A., Long K. S., Miller L., Turner T. J., 2008, *MNRAS* 388, 611
- Sim S. A., Miller L., Long K. S., Turner T. J., Reeves J. N., 2010, *MNRAS* 404, 1369
- Sim S. A., Proga D., Kurosawa R., Long K. S., Miller L., Turner T. J., 2012, *MNRAS* 426, 2859
- Simon L. E., Hamann F., 2010, *MNRAS* 409, 269
- Sluse D., Hutsemékers D., Anguita T., Braibant L., Riaud P., 2015, *ArXiv e-prints*
- Springel V., Di Matteo T., Hernquist L., 2005, *ApJ Letters* 620, L79
- Sutherland R. S., 1998, *MNRAS* 300, 321
- Tombesi F., Cappi M., Reeves J. N., Palumbo G. G. C., Yaqoob T., Braitto V., Dadina M., 2010, *A&A* 521, A57
- Turner T. J., Miller L., 2009, *AAPR* 17, 47
- Šurlan B., Hamann W.-R., Kubát J., Oskinova L. M., Feldmeier A., 2012, *A&A* 541, A37
- Verner D. A., Ferland G. J., Korista K. T., Yakovlev D. G., 1996, *ApJ* 465, 487
- Wei Z., 1988, *Astrophysical Letters and Communications* 27, 275
- Weymann R. J., Morris S. L., Foltz C. B., Hewett P. C., 1991, *ApJ* 373, 23
- Weymann R. J., Scott J. S., Schiano A. V. R., Christiansen W. A., 1982, *ApJ* 262, 497

Zhang S. N., Cui W., Chen W., 1997, ApJ Letters 482, L155

Zhou H., Wang T., Wang H., Wang J., Yuan W., Lu Y., 2006, ApJ 639, 716

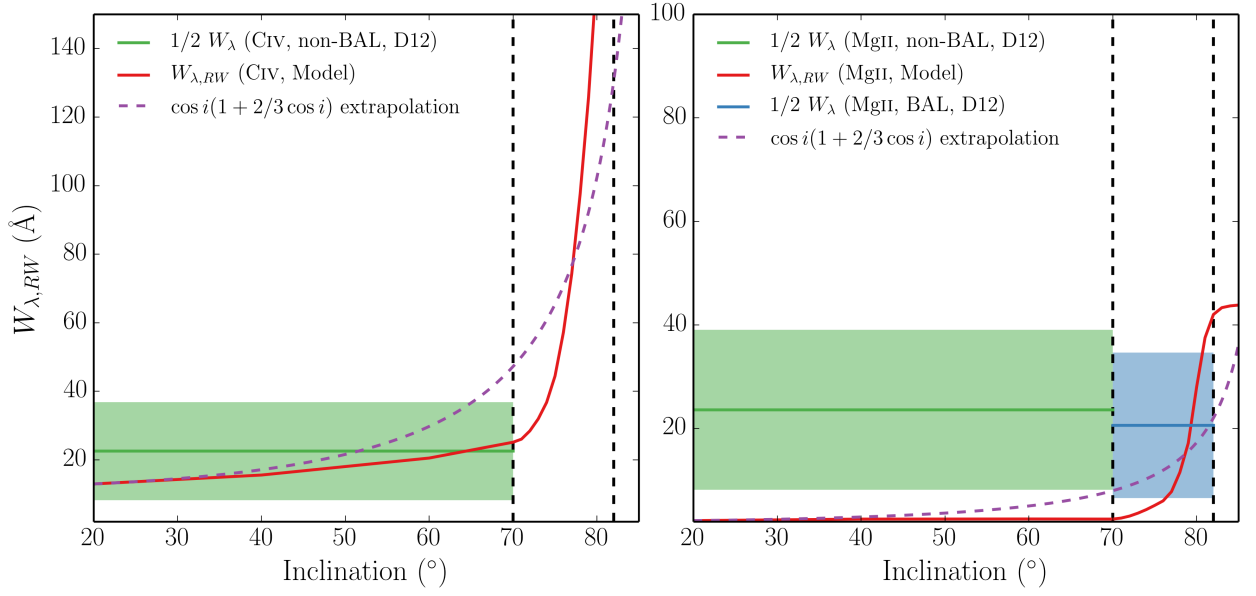


Fig. 6.— Physical properties of the outflow, shown by the coloured contours. The solid black line marks a sphere at $1000 r_G$. The dotted lines show the 72° and 78° sightlines to the centre of the system, and illustrate that different sightlines intersect material of different ionization states.

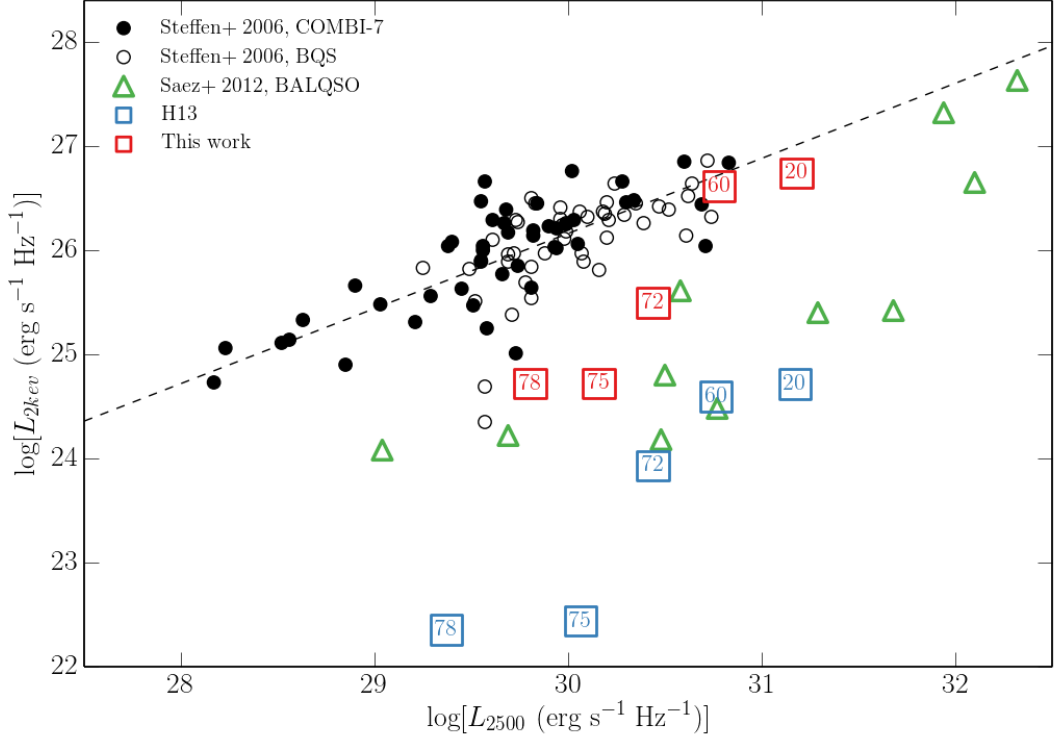


Fig. 7.— X-ray (2 keV) luminosity of the our clumped model (red squares) and the H13 model (purple squares), plotted against monochromatic luminosity at 2500Å. The points are labeled according to inclination; angles $> 70^\circ$ correspond to BALs in our scheme (see figure 4). Also plotted are the samples considered by Saez et al. 2012 on a similar plot; The COMBI-7 AGN and the BQS samples Steffen et al. (2006) and the Saez et al. (2012) sample of BALQSOs. The dotted line shows the best fit relation for non-BALQSOs from Steffen et al. (2006).

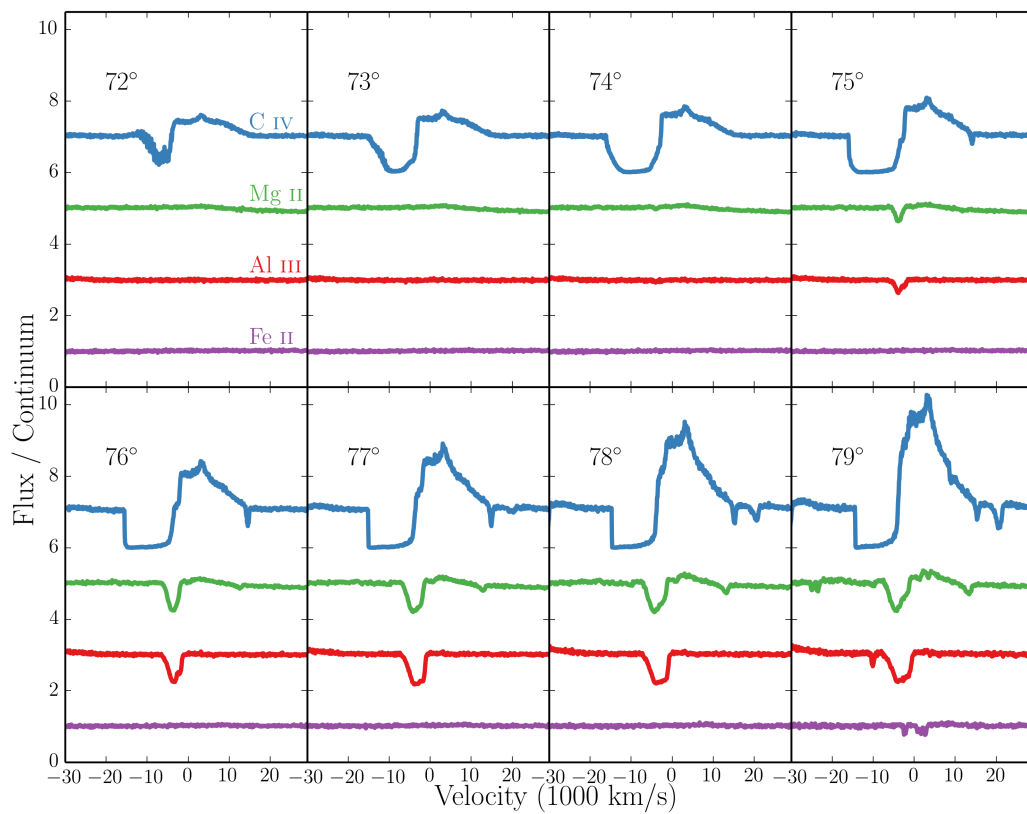


Fig. 8.— C IV, Mg II, Al III and Fe II line profiles for viewing angles from 72 – 79°. The profiles are plotted relative to the local continuum with an offset applied for clarity. Lower ionization profiles appear at a subset of high inclinations, compared to the ubiquitous C IV profile.